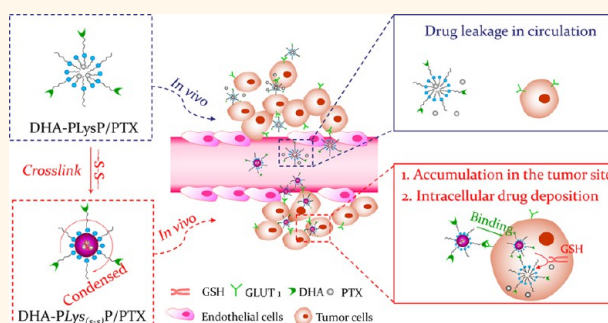# Smart Nanodevice Combined Tumor-Specific Vector with Cellular Microenvironment-Triggered Property for Highly Effective Antiglioma Therapy

Kun Shao,[†,‡] Ning Ding,[†,§] Shixian Huang,[†,‡] Sumei Ren,[†,§] Yu Zhang,[†,‡] Yuyang Kuang,[†,‡] Yubo Guo,[†,‡] Haojun Ma,[†,‡] Sai An,[†,‡] Yingxia Li,[†,§] and Chen Jiang[†,‡,*]

[†]Key Laboratory of Smart Drug Delivery, Ministry of Education, [‡]Department of Pharmaceutics, School of Pharmacy, and [§]Department of Medical Chemistry, School of Pharmacy, Fudan University, Shanghai 201203, People's Republic of China

**ABSTRACT** Malignant glioma, a highly aggressive tumor, is one of the deadliest types of cancer associated with dismal outcome despite optimal chemotherapeutic regimens. One explanation for this is the failure of most chemotherapeutics to accumulate in the tumors, additionally causing serious side effects in periphery. To solve these problems, we sought to develop a smart therapeutic nanodevice with cooperative dual characteristics of high tumor-targeting ability and selectively controlling drug deposition in tumor cells. This nanodevice was fabricated with a cross-linker, containing disulfide linkage to form an inner cellular microenvironment-responsive "-S-S-" barrier, which could shield the entrapped drug leaking in blood circulation. In addition, dehydroascorbic acid (DHA), a novel small molecular tumor-specific vector, was decorated on the nanodevice for tumor-specific recognition *via* GLUT1, a glucose transporter highly expressed on tumor cells. The drug-loaded nanodevice was supposed to maintain high integrity in the bloodstream and increasingly to specifically bind with tumor cells through the association of DHA with GLUT1. Once within the tumor cells, the drug release was triggered by a high level of intracellular glutathione. When these two features were combined, the smart nanodevice could markedly improve the drug tumor-targeting delivery efficiency, meanwhile decreasing systemic toxicity. Herein, this smart nanodevice showed promising potential as a powerful platform for highly effective antiglioma treatment.

**KEYWORDS:** polymeric micelles · dehydroascorbic acid · GLUT1 · cellular microenvironment · antiglioma · glutathione triggered · U87 xenograft model

Glioma is the most common high-grade primary brain tumor in adults with high morbidity and mortality.[1] A crucial challenge for glioma treatment is to deliver drugs effectively to invasive glioma cells residing in a sanctuary within the central nervous system (CNS).[2] The blood-brain barrier (BBB) restricts the delivery of most small and large therapeutic molecules into the brain.[3,4] Moreover, even though BBB is compromised to some extent in malignant glioma, it remains an obstacle influencing the glioma efficacy of antitumor drugs *via* systemic administration.[5] Various strategies such as temporary disruption of BBB as well as chemical modification of

available chemotherapeutic agents have been utilized to improve the antiglioma effect.[6−8] However, the treatment effect remains unsatisfied in the recent improvements.[6] Fortunately, there are many endogenous transport systems overexpressed on the BBB and glioma cells that can mediate ligand-modified drug delivery systems targeting glioma and enhancing antitumor drug uptake, which is regarded as a promising new method against the mentioned problems.[5,6]

To curb tumor progress with a tumor-specific manner is a long sought-after goal in oncotherapy. The limitation of chemotherapeutic agents has restricted their

clinical use, such as poor solubility, quick clearance, systemic toxicity, or development of multidrug resistance. More recently, designable nanoparticles (NPs) have gained much attention in chemotherapy due to their optimized size and functionalized surface characteristics.[9]

Specific ligands functionalizing on the NP surfaces have been used to improve tumor-targeting *via* receptor-mediated pathway, and it has been known that various transporters overexpressed on the tumor cell membranes aim to supply the excess nutritional needs of the tumor.[10] Compared to the receptor-mediated pathway, the transporter-mediated pathway is faster, has better efficiency, and is less impacted by endogenous substrates.[4,11] However, highly effective tumor-targeting NPs by the transporter-mediated pathway have not been widely developed.[12−15]

Facilitative glucose transporter isoform 1 (GLUT1) is a representative member in the GLUT family. It is mainly responsible for "two-way" transportation of D-glucose to keep its stable concentration in cells. This transporter is wildly distributed in normal tissues, such as blood-brain barrier, erythrocytes, and kidneys.[16] However, tumor cells deviating from most normal tissues exhibit a dysfunctional and ravenous consumption of glucose, known as Warburg effect.[17] It has proved that huge glucose consumption is an advantage for tumor cell proliferation in normoxic or hypoxic environments to evade killing by the immune system.[18,19] The molecular mechanisms underlying the Warburg effect have been elucidated, most notably that tumor cells overexpress the glucose transporter GLUT1.[20] Utilizing GLUT1 as targeted site such as FDG-PET has been applied in clinical tumor diagnosis.[21] In this article, this key discriminator of tumors from normal tissues was exploited as a targeted site for antiglioma.

Dehydroascorbic acid (DHA) is also one substrate of GLUT1 (Figure 1A).[22,23] The possibility is that a DHA molecule forms a hydrate and cyclizes to the bicyclic hemiketal form *in vivo*, which is structurally similar to D-glucose and is transported by GLUT1, as well (Figure 1A).[24] As reported, GLUT1 overexpressed on tumor cells can promote influx of DHA *via* facilitated diffusion.[25] Once inside the cell, DHA is rapidly reduced to ascorbate, which effectively is "trapped" within the cell (Figure 1A).[26] Thus, unlike the "two-way" transportation of D-glucose by GLUT1, it is like a "one-way" continuously accumulative process for DHA. Meanwhile, owing to the virtual absence of sodium ascorbate cotransporters (mainly transport Vc), DHA is the main substitute in obtaining and accumulating Vc for tumor cells.[27] Therefore, DHA is regarded as a potentially functional small molecule owing to high priority in tumor-specific recognition and transportation.

Polymeric micelles have been used to encapsulate and protect diverse small molecules, especially
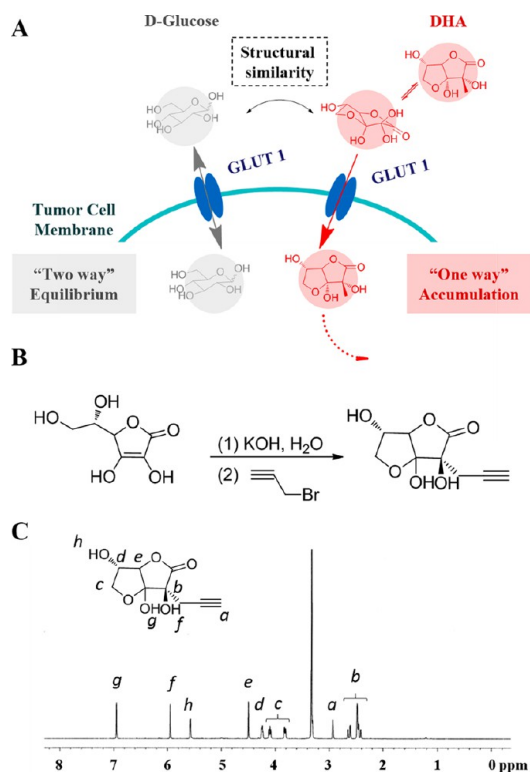


**Figure 1. (A) Different transportation characteristics of D-glucose and DHA by GLUT1. (B) Synthesis of propargyl-substituted DHA. (C) Characterization of propargyl-substituted DHA by $^1$H NMR spectrum in $D_2O$.**

hydrophobic drugs. Moreover, they have shown better deep penetrating ability and accumulating ability in tumors due to their smaller particle size (<100 nm).[28] This is an important advantage to treat glioma, in which the pore size of fenestrated capillary walls is smaller than other tumors and restricts larger particle leakiness.[29] Nevertheless, one of the biggest challenges conventional polymeric micelles face in *in vivo* application is the low structural stability. The stability of the existing micelles mainly relies on the hydrophobic interaction (physical interaction) between the drug and hydrophobic segment of amphipathic copolymers. This weak noncovalent bond hardly remains stable in blood circulation, which simply causes drug leaking from the micelles before reaching the targeted site. In our study, we attempted to introduce a covalent linkage between the polymers beyond the hydrophobic interaction, which could markedly increase structural stability of micelles.

It is noteworthy that the level of glutathione (GSH) in tumor cellular microenvironment is about 5000-fold higher than that in extracellular matrix.[30] GSH can cleave disulfide efficiently. The drug release triggered by GSH from disulfide bond cross-linked NPs has been developed.[31,32] In this article, a smart "anti-leakage barrier" based on disulfide bonds was introduced into the cores of polymeric micelles. This barrier was able to stabilize the structure of micelles, preventing the drug

loss in undesired sites in blood circulation. Once internalized into the targeted cells, disulfide bonds should be cleaved under higher GSH condition and the drugs would be released by a cellular microenvironment-triggered mechanism.

Herein, we aimed to develop glioma-targeting and GSH-triggered drug-releasing micelles, DHA-P$Lys_{(s-s)}$P. PEG-$p$Lys-$p$Phe was designed as an amphiphilic polypeptide copolymer to load the antitumor drug paclitaxel (PTX). We constituted the anti-leakage barrier by cross-linking the $p$Lys segment, which could stabilize the micellar structure in blood circulation and release the cargo quickly in the tumor cellular microenvironment. In addition, DHA was covalently anchored on the micelle surfaces via Click reaction. DHA-P$Lys_{(s-s)}$P micelles could significantly improve tumor accumulation of the drug. The improved antitumor efficacy was achieved by combining the tumor-specific recognition with cell-selective drug deposition.

## RESULTS AND DISCUSSION

The stability and targeting efficiency of drug nanocarriers are equally important for tumor-targeting therapy. Especially for chemotherapeutic agent delivery, undesirable drug loss in blood would cause serious systemic toxicity by nonspecific drug accumulation in normal tissues. In this work, we engineered a smart polymeric micelle system, DHA-P$Lys_{(s-s)}$P micelles, to achieve targeting to glioma and controlling antitumor drug release. DHA could actively guide the micelles to accumulate in the tumor site via GLUT1 binding. Additionally, drug deposition was controlled via the disulfide bond cross-linked barrier, which could protect drug leakage against blood dilution. Once entering cells, drug release was triggered by a high level of GSH. Combining tumor-specific recognition with cell-selective drug deposition, PTX could be delivered into glioma with higher efficiency and less side effects.

**Synthesis of DHA.** In contrast with D-glucose, DHA showed higher priority in tumor-targeting owing to its "one-way" accumulative process by GLUT1 transport (Figure 1A).[26] Herein, in order to modify DHA on micelle surfaces via Click reaction,[33] we introduced a propargyl group into the DHA molecule. As shown in Figure 1B,C, we successfully synthesized propargyl DHA. Additionally, $[M + H]^+$ was 214.5, calculated by mass spectrometry (Agilent, USA).

**Chemical Synthesis of Polypeptide Copolymers.** The polypeptide copolymers, CH$_3$O-PEG-$p$Lys-$p$Phe or N$_3$-PEG-$p$Lys-$p$Phe, were synthesized via two-step ring-opening polymerization (ROP) reaction in the presence of CH$_3$O-PEG-NH$_2$ or N$_3$-PEG-NH$_2$ as the initiator and N-carboxyanhydride (NCA) monomers of amino acids, Lys(Z)-NCA (**1**) and Phe-NCA (**2**) (Supporting Information, Scheme S1 and Scheme S2).[34,35] The introduction of an azide group to the end of the PEG chain was completed by the conversion of hydroxy of HO-PEG-NH$_2$ to give N$_3$-PEG-NH$_2$, according to the literature.[36] Here, the azide group at the N$_3$-PEG-$p$Lys-$p$Phe terminus provided an opportunity to install selectively an alkynyl moiety via Click reaction.[33] The triblock copolymers, PEG-$p$Lys-$p$Phe, were designed with three segments, which played different roles in forming micelles: (1) $p$Phe, the hydrophobic core for insoluble drug entrapped; (2) $p$Lys, the naked amino groups on side chains for cross-linking reaction; (3) PEG, for prolonging circulation time and surface functionalization.

The conversion of monomeric Lys(Z) and Phe to polymeric $p$Lys(Z) and $p$Phe was 83.3%, consistent with previous studies.[35] The ability to control the molecular weight distribution makes NCA-based polymerization advantageous for bioconjugation.[37] The molar composition ratio of EG to Lys and Phe was 113:10:20, calculated by $^1$H NMR after purification in every step of polymerization (Figure 2B(a,b)). The complete disappearance of the resonance peak from methylene protons ($-$CH$_2$Ph) of $p$Lys(Z) blocks at 5.12 ppm demonstrated that the Z group was removed from $p$Lys-(Z) successfully (Figure 2B(c)). The molecular weight calculated by $^1$H NMR was 9939.37. Additionally, the IR spectra demonstrated that the conversion and polymerization of amino acid monomers were successful (Supporting Information, Figure S1).

Conjugation of DHA to the distal end of copolymers was performed via copper(I)-catalyzed azide−alkyne Click reaction.[33,38] Propargylic DHA could react with the azide moiety of N$_3$-PEG-$p$Lys-$p$Phe in the presence of Cu(I) catalyst to form a triazole, which is very stable in physiological conditions (Figure 2A). Click reaction is a preferable approach for bioconjugation because the process is fast, highly efficient, and completed under a mild condition.[38] As shown in the $^1$H spectra (Figure 2B(d)), peaks at 8.4−8.7 ppm (d) indicated the presence of a triazole ring formed in the Click reaction, and the conjugation of DHA to the copolymers was successful.

**Formulation and Characterization of PTX-Loaded DHA-P$Lys_{(s-s)}$P Micelles.** The drug-loaded DHA-P$Lys_{(s-s)}$P micelles were prepared using a dialysis method with a drug/copolymer mixture (Figure 3A).[34,35] The quantitative addition of functionalized copolymers DHA-PEG-$p$Lys-$p$Phe could control the density of DHA at the micelle surfaces.[39] In this work, four kinds of polymeric micelles were prepared: DHA-modified cross-linked or non-cross-linked micelles (DHA-P$Lys_{(s-s)}$P/PTX or DHA-PLysP/PTX) and unmodified cross-linked or non-cross-linked micelles (P$Lys_{(s-s)}$P/PTX or PLysP/PTX). To build a smart anti-leakage barrier, intramicellar disulfide linkage was established between amino groups of $p$Lys segments by NHS groups of DTSSP (Figure 3A).

AFM images showed that both of the DHA-PLysP/PTX and DHA-P$Lys_{(s-s)}$P/PTX micelles revealed a regular
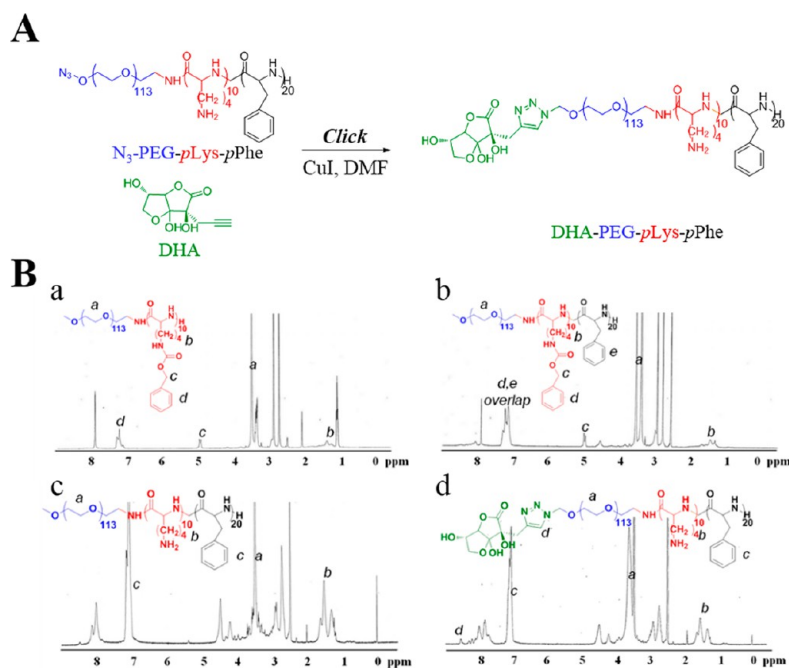
**Figure 2.** (A) Synthesis of modification of N$_3$-PEG-*p*Lys-*p*Phe with DHA through Click reaction. (B) Characterization of polypeptide copolymers. $^1$H NMR spectrum of CH$_3$O-PEG-*p*Lys(Z) (a), CH$_3$O-PEG-*p*Lys(Z)-*p*Phe (b), CH$_3$O-PEG-*p*Lys-*p*Phe (c), and DHA-PEG-*p*Lys-*p*Phe (d) recorded in DMSO-*d*$_6$.
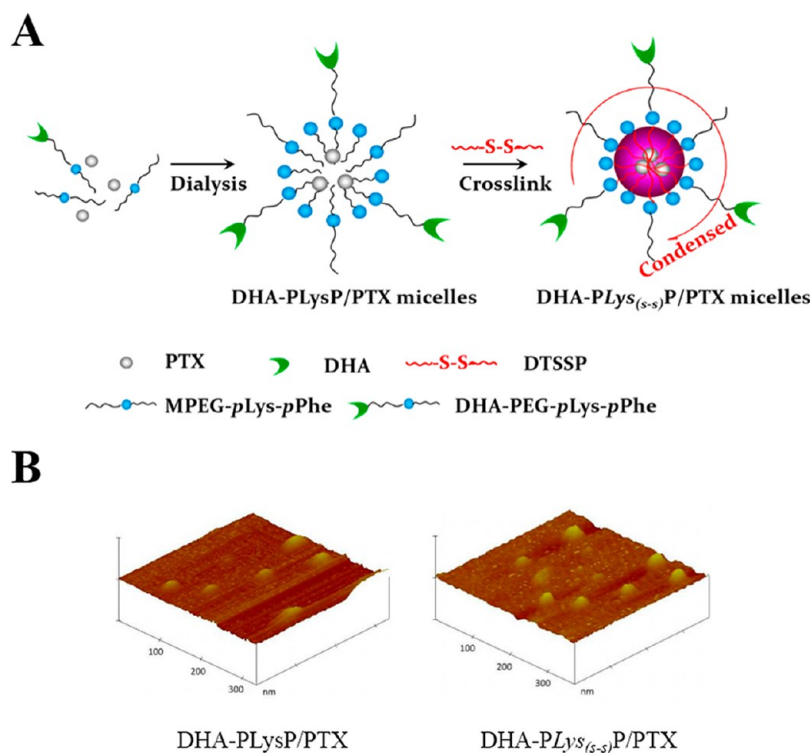


**Figure 3.** (A) Stepwise synthesis of the PTX-loaded DHA-P*Lys*$_{(s\text{-}s)}$P micelles. (B) AFM images of DHA-PLysP/PTX (left) and DHA-P*Lys*$_{(s\text{-}s)}$P/PTX (right) micelles.

spherical morphology in uniform particle sizes with high dispersivity (Figure 3B). There was no aggregation caused by cross-linking reaction. Notably, zeta-potentials of DHA-P*Lys*$_{(s\text{-}s)}$P/PTX were lowered significantly compared to those of DHA-PLysP/PTX (Table 1).

It suggested that the primary amino groups of the *p*Lys segment were converted to amino linkages and the free amino groups were decreased.[34] The particle sizes of DHA-P*Lys*$_{(s\text{-}s)}$P/PTX were also smaller after cross-linking, as well (Table 1). It indicated that the structure

of DHA-PLys$_{(s-s)}$P/PTX became much more condensed (Figure 3A) after cross-linking. There were two possible reasons: (1) decreased primary amino groups of $p$Lys segments could reduce the intermolecular electrostatic repulsion; (2) disulfide network formation could decrease the intermolecular distance of copolymers. Simultaneously, the drug entrapping efficiency and loading efficiency of DHA-PLys$_{(s-s)}$P/PTX were 92 and 4.6%, respectively. Additionally, we evaluated the cross-linked micelles' *in vitro* stability by GSH-responsive drug release assay. When exposed to the medium of GSH-free or low GSH concentration (2 $\mu$M, extracellular GSH level), it showed that DHA-PLys$_{(s-s)}$P micelles remained stable with only 20% 6-coumarin release within 48 h. As the GSH concentration increased up to the cytoplasm level (10 mM), the release of 6-coumarin was markedly facilitated. These findings suggested that the DHA-PLys$_{(s-s)}$P micelles were very stable in the extracellular environment. However, the drug release was initiated once entering the cells (data not shown).

**Investigation of Cellular Uptake and Internalization Mechanism.** U87 cells, human-derived malignant glioma cells, were good candidate as *in vitro* model because their

surfaces highly express GLUT1.[40] The cellular uptake characteristics and mechanisms were investigated *in vitro* by Red-BODIPY ($\lambda_{ex}$ = 650 nm, $\lambda_{em}$ = 665 nm) labeling (Figure 4). Compared with PLys$_{(s-s)}$P micelles, the internalization of DHA-PLys$_{(s-s)}$P micelles was significantly enhanced with increasing DHA modification (from 10 to 40 mol %) (Figure 4A−D). The results suggested that DHA could change the fate of the micelles due to selectively targeting glioma cells. As expected, propargyl-modified DHA retained its transportation ability *via* GLUT1. Additionally, it retained the targeting activity when being decorated on the micelles (Figure 4A−D).

To investigate internalization mechanisms of DHA-PLys$_{(s-s)}$P micelles, the endocytosis pathways were inhibited by various inhibitors,[41] including 10 mM D-glucose (GLUT1) (Figure 4G), 0.5 $\mu$g/mL filipin (Fil, caveolae-mediated pathway) (Figure 4E), 2.5 $\mu$M phenyl-arsine oxide (PhO, clathrin-dependent pathway), 2.5 $\mu$M colchicines (Col, macropinocytosis). The internalization of DHA-PLys$_{(s-s)}$P micelles was inhibited significantly by 10 mM D-glucose (Figure 4G) and 0.5 $\mu$g/mL Fil (Figure 4E). It indicated that the endocytic pathway of DHA-PLys$_{(s-s)}$P micelles mainly referred to the caveolae-mediated pathway, which was similar with common micelles. Additionally, low temperature remarkably inhibited the cellular uptake, as well (Figure 4I), demonstrating that the internalization pathway was energy-dependent. Considering these findings, it was suggested that DHA was mainly responsible for recognizing and binding with GLUT1, whereas the natural properties of micelles, such as size and surface features,

**TABLE 1. Summary of Nanoparticle Properties**

| polymeric micelles | size ($d$, nm)$^a$ | PDI | zeta-potential (mV)$^a$ |
|---|---|---|---|
| DHA-PLysP/PTX | 59 ± 4 | 0.11 ± 0.01 | 14.1 ± 1.1 |
| DHA-PLys$_{(s-s)}$P/PTX | 47 ± 3 | 0.09 ± 0.03 | 2.35 ± 0.1 |

$^a$ Determined by Zetasizer Nano.
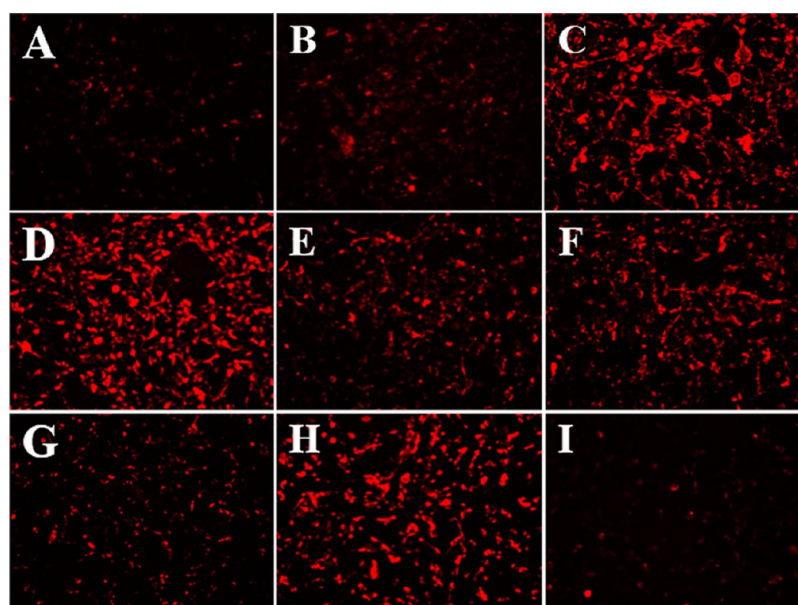


**Figure 4. Cellular uptake of PLys$_{(s-s)}$P micelles (A) and DHA-PLys$_{(s-s)}$P micelles with DHA modification ratio of 10 mol % (B), 20 mol % (C), and 40 mol % (D). The micelles were labeled by Red-BODIPY. (D−I) Possible involved pathway of DHA-PLys$_{(s-s)}$P micelle entry into U87 was observed by fluorescence microscopy qualitatively. The cells were blocked by different inhibitors (E, 0.5 $\mu$g/mL Fil; F, 2.5 $\mu$M PhO; G, 10 mM D-glucose; H, 2.5 $\mu$M Col). The cells incubated with DHA-PLys$_{(s-s)}$P in the absence of any inhibitor (D) were considered as control. (I) Cells were incubated with DHA-PLys$_{(s-s)}$P micelles at 4 °C.**
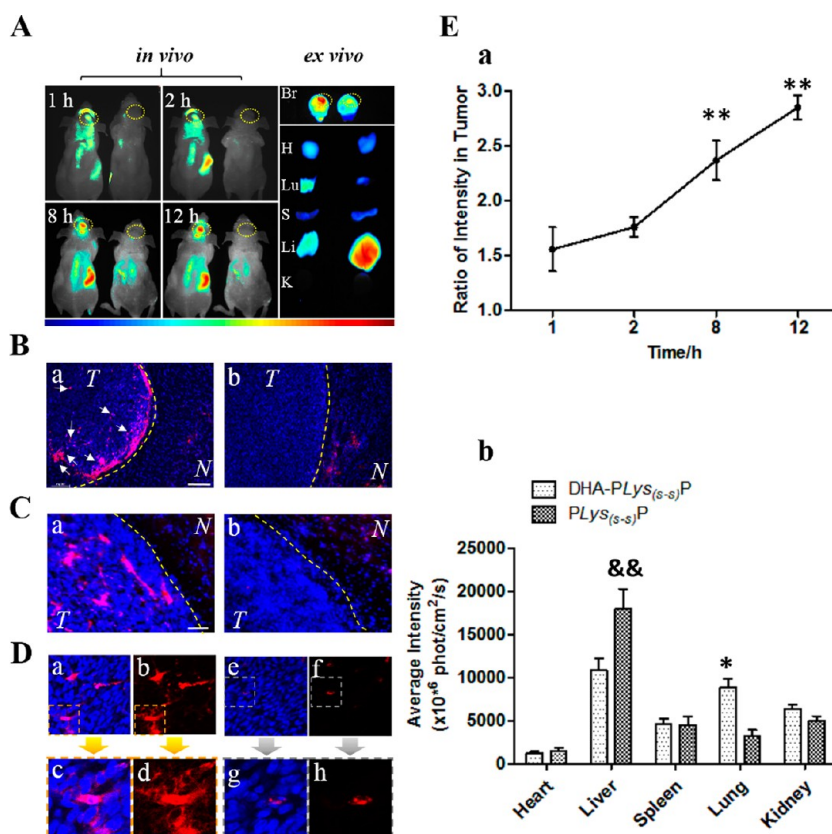
**Figure 5.** *In vivo* distribution and subcellular location of DHA-P*Lys*$_{(s-s)}$P micelles on the U87 xenograft model. (A) Representative real-time fluorescence imaging of mice treated with Red-BODIPY-labeled DHA-P*Lys*$_{(s-s)}$P (left in every image) or P*Lys*$_{(s-s)}$P (right in every image) micelles. *In vivo* images were taken at 1, 2, 8, and 12 h after i.v. injection. *Ex vivo* images showed the corresponding exposed main organs (glioma-bearing brain, Br; heart, H; liver, L; spleen, S; lung, L; kidney, K) that were excised 12 h after administration. Intensity of the signal: dark red is the strongest, while dark blue is the weakest, as shown by the bar. (B) Fluorescence microscopic imaging of glioma-bearing brain sections showed the increasingly accumulation of DHA-P*Lys*$_{(s-s)}$P micelles (a) both at interior and margin of the glioma, compared to P*Lys*$_{(s-s)}$P micelles (b). N = normal brain; T = tumor; yellow dashed line = boundary of the glioma; red, Red-BODIPY-labeled micelles; blue, DAPI-stained cell nuclei; white arrow probed the signals from DHA-P*Lys*$_{(s-s)}$P micelles; original magnification = 50×. (C) Confocal microscopic imaging of glioma-bearing brain sections. Original magnification = 200×. (D) Corresponding subcellular localization of DHA-P*Lys*$_{(s-s)}$P (a,b) or P*Lys*$_{(s-s)}$P (e,f) micelles within the glioma. The region in the dotted box was enlarged and shown in c,d or g,h, respectively. (E) Quantitative analysis of glioma target ability (a) and *in vivo* distribution (b) of DHA-P*Lys*$_{(s-s)}$P micelles. (a) Signal intensity ratio in the tumor area (DHA-P*Lys*$_{(s-s)}$P *versus* P*Lys*$_{(s-s)}$P treated group) at different time points. (b) *In vivo* distribution of micelles 12 h after administration (*$p < 0.05$, **$p < 0.01$, DHA-P*Lys*$_{(s-s)}$P vs P*Lys*$_{(s-s)}$P; &&$p < 0.01$, P*Lys*$_{(s-s)}$P vs DHA-P*Lys*$_{(s-s)}$P; n = 3).

played an important role in DHA-P*Lys*$_{(s-s)}$P micelle internalization. This pattern was different from the simple receptor-mediated clathrin-dependent pathway. Additionally, we obtained a similar conclusion from the assessments on brain capillary endothelial cells (BCECs), which highly express GLUT1, as well (data not shown).

**Evaluation of Glioma-Targeting Effect and *In Vivo* Distribution.** To evaluate the glioma-targeting effect, Red-BODIPY-labeled DHA-P*Lys*$_{(s-s)}$P or P*Lys*$_{(s-s)}$P micelles were i.v. injected into glioma-bearing mice. DHA-P*Lys*$_{(s-s)}$P micelles showed a progressive accumulation in glioma from 1 to 12 h after administration (Figure 5A). The signal intensity ratio in the glioma area (DHA-P*Lys*$_{(s-s)}$P *versus* P*Lys*$_{(s-s)}$P treated group) at different time points was analyzed quantitatively. Compared to P*Lys*$_{(s-s)}$P, DHA-P*Lys*$_{(s-s)}$P exhibited much higher targeting effiency in glioma sites (Figure 5E(a)). Notably, the

targeting efficiencies of DHA-P*Lys*$_{(s-s)}$P micelles were 2.36- (**$p < 0.01$) and 2.84-fold (**$p < 0.01$) higher than that of the P*Lys*$_{(s-s)}$P treated group at 8 and 12 h, respectively. Above all, DHA maintained the high glioma-targeting ability *in vivo*, which could promote the micelles gradually accumulating in glioma.

In order to further study the *in vivo* subcellular localization of micelles, the glioma-bearing brains were observed under fluorescence microscopy (Figure 5B) and confocal microscopy (Figure 5C,D). The localizations of micelles at the glioma in low-magnification images were obtained from fluorescence microscopy. As shown in Figure 5B,C, overwhelming majority of micelles were accumulated in glioma boundaries and a portion of them were localized in the glioma central region in the DHA-P*Lys*$_{(s-s)}$P treated group. Most importantly, DHA-P*Lys*$_{(s-s)}$P micelles could be readily further internalized into glioma cells (Figure 5D).

As reported, tumor microenvironment becomes one of the greatest difficulties for a drug to deeply penetrate into the tumor central region because of higher pressure and hypoxia.[42−44] Recently, it has been demonstrated that the expression levels of GLUT1 were highly up-regulated in the intratumoral region as the tumor developed.[44] Accordingly, the uptake of D-glucose increased. Meanwhile, as indicated in our study, we could see notably intratumoral accumulation of DHA-PLys$_{(s-s)}$P micelles, compared with PLys$_{(s-s)}$P micelles. All of these findings revealed that DHA could provide a promising potential to increase the tumor penetration ability of nanoparticles.

As shown in *ex vivo* images, there was higher accumulation in the liver of mice treated with PLys$_{(s-s)}$P micelles (1.7-fold, [&&]$p < 0.01$, *vs* DHA-PLys$_{(s-s)}$P treated group, Figure 5E(b)). This was probably attributed to the properties (sizes and zeta-potential, *etc.*) of micelles composed of polypeptides.[45] However, besides higher accumulation in the glioma, the drug distribution was relatively lower in liver and partially higher in lung for the DHA-PLys$_{(s-s)}$P treated group. It was demonstrated that the distribution and clearance of micelles *in vivo* were altered after modifying with DHA on the surfaces of micelles. Meanwhile, the fluorescence signal was visible in the intestinal tract in the DHA-PLys$_{(s-s)}$P treated group (Figure 5A, left). It suggested that DHA-PLys$_{(s-s)}$P micelles were further excreted into the intestine from the liver, evidenced by the decreased accumulation in the liver. Additionally, the signals of kidneys (both groups) after 12 h administration were very weak. This was attributed to the different excretion pathway between micelles and small molecular drugs.[46] The possible excretion pathway of micelles was mainly through the liver. Another possibility was that the excretion by kidneys was completed 12 h after administration.

***In Vitro* Evaluation of Antiglioma Effect.** The antitumor effect of DHA-PLys$_{(s-s)}$P/PTX micelles was evaluated *in vitro* on human glioma U87 cells through a cell viability assay, an antiproliferation assay, and cellular apoptosis by TUNEL assay.

Cell viability assay (Figure 6A) showed that the IC$_{50}$ value of Taxol on U87 cells after 48 h incubation was 0.3067 $\mu$M, similar to previous reports.[47,48] IC$_{50}$ values of PLysP/PTX and PLys$_{(s-s)}$P/PTX were 0.388 and 0.397 $\mu$M, respectively, and slightly higher than that of the Taxol treated group. This was because Taxol and its micellar formulations had a different pathway to enter into cells. Taxol could more readily enter tumor cells *via* passive diffusion,[49] whereas micelles were mainly internalized through an endocytotic pathway (Figure 4). Furthermore, the statistically lower IC$_{50}$ value was provided at 0.2314 $\mu$M (***$p < 0.001$ *vs* Taxol; [&&&]$p < 0.001$ *vs* PLys$_{(s-s)}$P/PTX; $n = 4$) in the DHA-PLys$_{(s-s)}$P/PTX treated group. This greatest cytotoxicity against U87 was mainly attributed to DHA modification, which

dramatically promotes DHA-PLys$_{(s-s)}$P/PTX uptake by tumor cells.

PTX could trigger cell cycle arrest on G2/M to induce robust mitotic delay through microtubule stabilization.[50,51] This means that the cellular apoptosis induced by PTX could probably have time lag. In our study, both cell viability assay and other cytotoxic assays (cell cycle test or Annexin V-FITC staining assays) aimed at reflecting the apoptotic effect *in vitro* induced by different PTX micellar formulations (Figure 6). G2/M arrests in U87 were investigated after 48 h treatment with PTX micelles to evaluate the antiproliferative activity (Figure 6B). G2/M fractions of U87 were increased significantly after treated with PTX micelles (21.82−48.04%) compared with the Taxol treated group (17.54%). G2/M fractions in groups exposed to cross-linked micelles (PLys$_{(s-s)}$P/PTX and DHA-PLys$_{(s-s)}$P/PTX) were slightly higher than that treated by non-cross-linked micelles (PLysP/PTX and DHA-PLysP/PTX). Additionally, the proportion of cells in sub-G1 fractions (14.54%) was increased because of dramatically abrogated delay of the cell cycle in the DHA-PLys$_{(s-s)}$P/PTX treated group (48.04%), which is considered a measure of nonviable cells (including apoptosis).[47]

Accordingly, to further characterize the apoptotic features of PTX micellar formulations, Annexin V-FITC staining assays were performed to indicate early apoptosis (green). Late apoptotic or necrotic cells were shown with PI staining (red). Compared to unmodified micelles, early apoptosis and late apoptosis were remarkably increased after 48 h treatment with DHA-modified micelles. Substantial apoptotic cells were revealed in the DHA-PLys$_{(s-s)}$P/PTX treated group, compared to PLys$_{(s-s)}$P/PTX or DHA-PLysP/PTX.

***In Vivo* Antitumor Efficacy.** Annexin-Vivo 750 was applied to show the apoptotic cells and revealed information about immediate cell death in a glioma model (Figure 7).[52] Compared with PLys$_{(s-s)}$P/PTX, apoptotic signals were achieved significantly in the DHA-PLys$_{(s-s)}$P/PTX treated group (Figure 7A,B). This result is consistent with high accumulation of DHA-PLys$_{(s-s)}$P/PTX within glioma cells *in vivo* (Figure 5). The apoptotic signals were further confirmed by TUNEL assay analysis (Figure 7C,D). Most importantly, these apoptotic cells were mainly distributed in the central glioma region, indicating that tumor permeability of DHA-modified micelles was improved by binding with GLUT1 (Figure 7C).

The therapeutic effects were evaluated by survival days in the glioma models, and weight loss could indicate the systemic toxicity from PTX to some extent.[53] The control group exhibited a rapid loss of body weight and early death (median survival, 23.5 days, Figure 8), consistent with previous studies.[54] Compared to the Taxol treated group (median survival, 25.5 days), micelle treated groups possessed prolonged survival times, and the loss in body weight
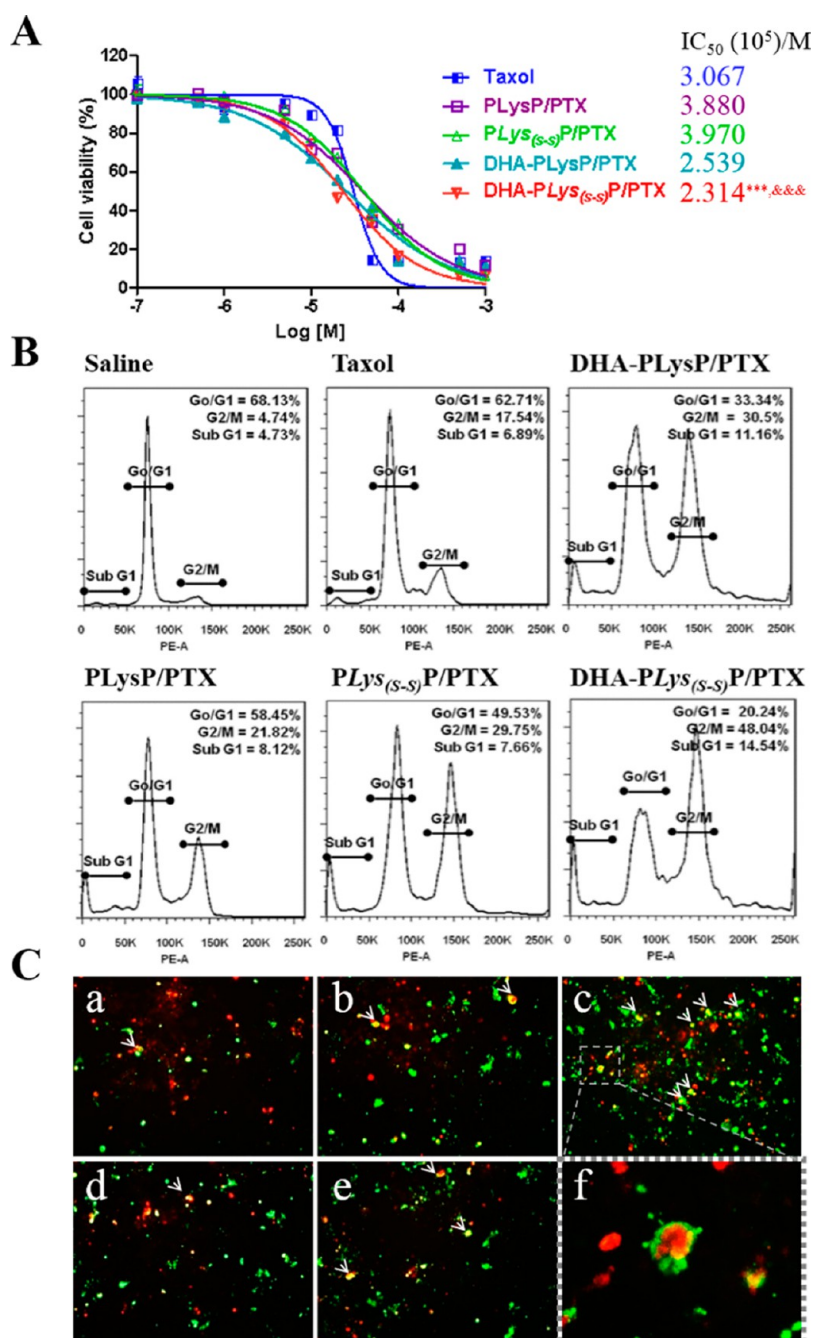
**Figure 6.** (A) Cell viability of treatment with different PTX formulations, Taxol, PLysP/PTX, P*Lys*$_{(s-s)}$P/PTX, DHA-PLysP/PTX, and DHA-P*Lys*$_{(s-s)}$P/PTX ($n = 4$). (B) Cellular mitotic delay induced by PTX and increased cell death. U87 cells were evaluated for cell cycle distribution *via* FACS analysis after 2 h of incubation in their culture medium added or not (control) with Taxol, DHA-PLysP/PTX, DHA-P*Lys*$_{(s-s)}$P/PTX, PLysP/PTX, and P*Lys*$_{(s-s)}$P/PTX micelles followed by another 48 h of incubation only in the culture medium. (C) Cellular apoptosis of U87 cells induced by Taxol (a), DHA-PLysP/PTX (b), DHA-P*Lys*$_{(s-s)}$P/PTX (c), PLysP/PTX (d), and P*Lys*$_{(s-s)}$P/PTX (e) was examined by fluorescence microscopy after 2 h treatment and 48 h incubation. (f) Enlarged view of dashed region in (c). Green, FITC-labeled apoptotic cells; red, PI-labeled apoptotic cells or dead cells.

was much gentler. Compared with nontargeted micelles (PLysP/PTX or P*Lys*$_{(s-s)}$P/PTX), DHA-PLysP/PTX and DHA-P*Lys*$_{(s-s)}$P/PTX possessed longer survival days. Additionally, the survival days were markedly prolonged in the DHA-P*Lys*$_{(s-s)}$P/PTX treated group and achieved the greatest antitumor efficacy. It indicated that the anti-leakage barrier of DHA-P*Lys*$_{(s-s)}$P/PTX altered distribution of PTX and markedly decreased

free PTX in the blood system *in vivo*, which increased drug accumulation in the glioma site and decreased PTX in periphery.

## CONCLUSION

A key issue in oncotherapy is how to enhance the tumor delivery efficiency of therapeutic agents, meanwhile decreasing side effects. It is practical to develop a
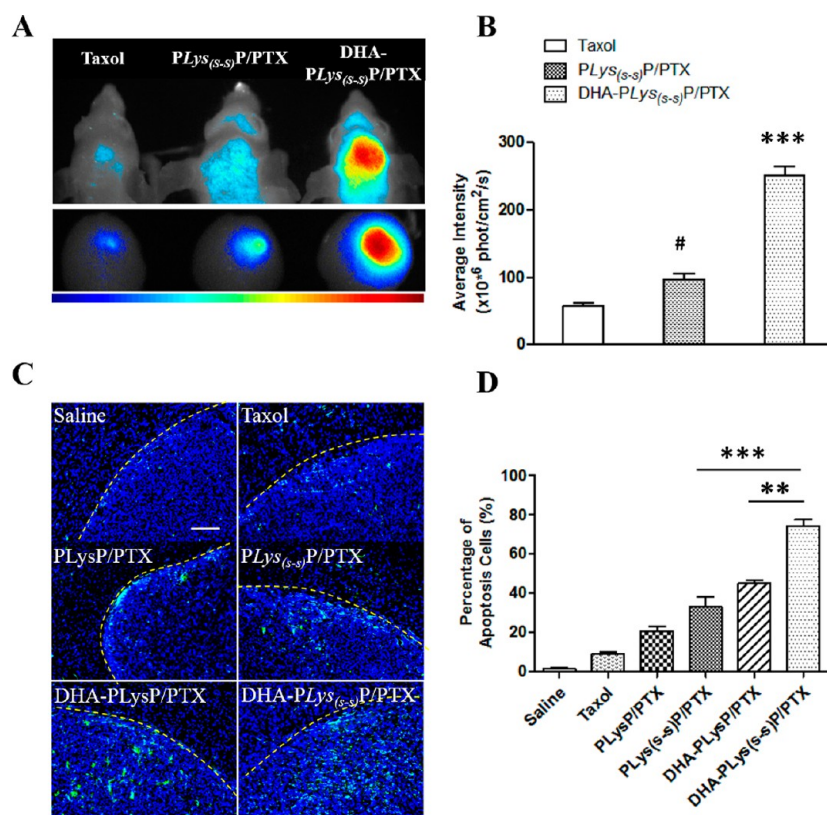
**Figure 7.** (A) Representative *in vivo* apoptosis images 24 h after Annexin-Vivo 750 administration after DHA-P$Lys_{(s-s)}$P/PTX (right), P$Lys_{(s-s)}$P/PTX (middle), and Taxol (left) treatment groups. (B) Quantitative analysis of apoptotic signal intensities of corresponding treated groups (***$p < 0.005$, DHA-P$Lys_{(s-s)}$P/PTX *vs* P$Lys_{(s-s)}$P/PTX; #$p < 0.05$, P$Lys_{(s-s)}$P/PTX *vs* Taxol; $n = 3$). (C) Representative histological images of the glioma-bearing brains using the TUNEL assay after Taxol, DHA-PLysP/PTX, PLysP/PTX, P$Lys_{(s-s)}$P/PTX, and DHA-P$Lys_{(s-s)}$P/PTX treatment. Saline treated group was considered as control. Blue, DAPI-stained cell nuclei; green, apoptosis cells; yellow dashed line, boundary of the glioma; original magnification = 100×. (D) Analysis of percentage of apoptosis cells (***$p < 0.005$, DHA-P$Lys_{(s-s)}$P/PTX *vs* P$Lys_{(s-s)}$P/PTX; **$p < 0.01$, DHA-P$Lys_{(s-s)}$P/PTX *vs* DHA-PLysP/PTX; $n = 3$).
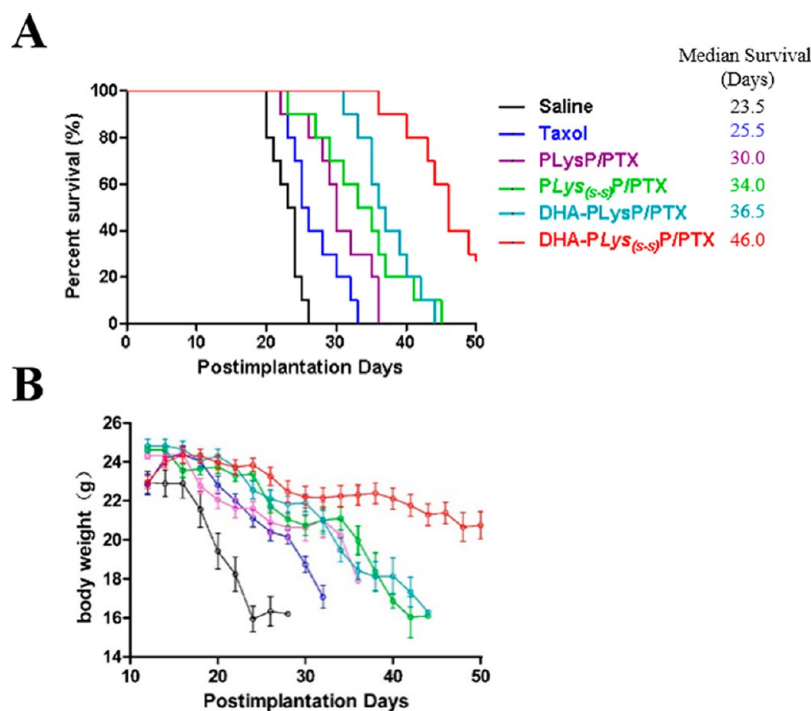


**Figure 8.** Kaplan−Meier survival curves (A) and average changes of body weight (B) of glioma-bearing mice treated with different PTX formulations at days 12, 15, and 18 postimplantation ($n = 15$).

powerful tumor-targeting drug delivery system. In this study, DHA was exploited as a novel targeting moiety, and smart and highly effective tumor-targeting DHA-P$Lys_{(s-s)}$P micelles were established for delivering antitumor drugs. In summary, DHA-P$Lys_{(s-s)}$P exhibited significantly stronger glioma-targeting ability, improved

tumor permeability, enhanced chemotherapeutic effect of PTX, and decreased side effects in glioma-bearing animal models. Due to the smart "-S-S-" barriers inside micelles, DHA-P$Lys_{(s-s)}$P was determined to have great potential as a carrier for chemotherapeutic drugs in tumor-targeting delivery.

## EXPERIMENTAL METHODS

**Materials.** $N^6$-Carbobenzyloxy-L-lysine $N$-carboxyanhydride (Lys(Z)-NCA) and L-phenylalanine $N$-carboxyanhydride (Phe-NCA) of high purity were used for the Fuchs–Farthing method using triphosgene (Supporting Information, Scheme S1).[55] 4,6-Diamidino-2-phenylindole (DAPI), 6-(((4,4-difluoro-5-(2-pyrrolyl)-4-bora-3a,4a-diaza-s-indacene-3-yl)styryloxy)acetyl)aminohexanoic acid, and succinimidyl ester (Red-BODIPY) were purchased from Molecular Probes (Eugene, OR, USA). 3,3′-Dithiobis(sulfosuccinimidylpropionate) (DTSSP) was purchased from PIERCE (Thermo, USA). Annexin-Vivo 750 was purchased from GE Healthcare (USA). D-Glucose, phenylarine oxide, filipin complex, and colchicines were purchased from Sigma-Aldrich (St. Louis, MO, USA). Taxol (dissolving PTX in Cremophor EL/EtOH 1:1) was further diluted by saline when used.

Balb-c nude mice (male, 18—20 g) were purchased from the Sino-British SIPPR/BK Lab Animal Ltd. (Shanghai, China). All animal experiments were carried out in accordance with guidelines evaluated and approved by Fudan University Institutional Animal Care and Use Committee (IACUC).

**Block Copolymer Synthesis.** CH$_3$O-PEG-$p$Lys-$p$Phe block copolymer, comprising EG units of 113 (MW 5000), Lys units of 10, and Phe units of 20, was synthesized via ROP reaction as previously described.[34,35] N$_3$-PEG-$p$Lys-$p$Phe was synthesized by the same procedure, with N$_3$-PEG-NH$_2$ (MW 5000) as an initiator. In brief, under a dry atmosphere, CH$_3$O-PEG-NH$_2$ or N$_3$-PEG-NH$_2$ (1 g, 0.2 mmol) was dissolved in anhydrous DMF (10 mL) with stirring. Lys(Z)-NCA (736 mg, 2.4 mmol) in anhydrous DMF was added into the PEG solution at 50 °C under argon. After 48 h, Phe-NCA (917 mg, 4.8 mmol) in anhydrous DMF was added to the reaction mixture. The reaction was maintained at 50 °C for another 48 h. The copolymer mixture was precipitated into diethyl either and was dried to yield an off-white solid. Yield 91%. Finally, the deprotection of PEG-$p$Lys(Z)-$p$Phe was performed by treating the block copolymer with TFA (10 mL) and HBr/HOAc (0.5 mL) to remove Z groups (Supporting Information, Scheme S1). PEG-$p$Lys-$p$Phe was isolated by dialysis using a membrane (Spectrapor, MWCO 1000) for 48 h, followed by freeze-drying. The preparation of fluorescently labeled CH$_3$O-PEG-$p$Lys-$p$Phe was achieved by the reaction of amino groups on side chains of $p$Lys with active groups contained in Red-BODIPY. Briefly, the CH$_3$O-PEG-$p$Lys-$p$Phe ($p$Lys, 10 amino groups) was dissolved in DMF with 0.1 equiv of probe solution and 0.5 equiv of triethylamine. The reaction was maintained at room temperature for 1 h and further purified by dialysis in the darkness.

DHA was coupled to the terminus of N$_3$-PEG-$p$Lys-$p$Phe via copper(I)-catalyzed azide—alkyne Click reaction.[56] The copolymer N$_3$-PEG-$p$Lys-$p$Phe (500 mg, 0.1 mmol) and excess azidated DHA (43 mg, 0.2 mmol, 2 equiv) were dissolved in 5 mL of DMF under argon. A freshly prepared solution of CuI (0.5 equiv) and DIPEA (1 equiv) was added, and the reaction was carried out for 12 h at 30 °C. The product DHA-PEG-$p$Lys-$p$Phe was purified by dialysis against 10 mM EDTA-2Na pH 7.0 for 24 h, deionized water for 24 h, followed by freeze-drying.

**Micelle Preparation.** The PTX-loaded polymeric micelles were prepared by dialysis method and a subsequent cross-linking reaction with slight modification.[34,35] In brief, CH$_3$O-PEG-$p$Lys-$p$Phe (10 mg) and 0.5 mg of PTX were dissolved in 0.5 mL of DMF. The solution was dialyzed against deionized water for 24 h using a membrane (MWCO 1000). Then the non-cross-linked PTX-loaded micelles, PLysP/PTX, were collected. For cross-linked micelle preparation, a disulfide-containing cross-linking

agent, DTSSP, was added into the solution at the feed molar ratio of [DTSSP]/[Lys] = 1:1. The reaction was maintained for 3 h at pH 8.0, and the solution was dialyzed for 3 h to remove residual DTSSP and unloaded PTX, which were P$Lys_{(s-s)}$P/PTX micelles. For DHA-modified micelle preparation, 40 mol % (of total copolymers) of DHA-PEG-$p$Lys-$p$Phe was added into the copolymer DMF solution. The later process was the same as mentioned above.

The empty micelles were prepared according to the protocol, without addition of PTX into the copolymer mixture in DMF. For Red-BODIPY-labeled micelle preparation, 0.5 mol % of fluorescently labeled CH$_3$O-PEG-$p$Lys-$p$Phe was added into the micelles composition.

**Micelle Characterization.** Micelles were analyzed by dynamic light scattering to determine size/PDI and zeta-potential. Results of size distribution were shown as the average diameter with PDI. The morphological examination of micelles was performed using atomic force microscopy (AFM, Veeco Instruments Inc., USA).

**Investigation of Cellular Uptake and Internalization Mechanism.** U87 cells were seeded in 24-well culture plates (Corning-Coaster, Tokyo, Japan) at a density of $2 \times 10^4$ cells/well. When 70—80% confluence was achieved, the cells were washed extensively and preincubated with PBS pH 7.4 for 15 min at 37 °C. Then the cells were incubated with the Red-BODIPY-labeled DHA-P$Lys_{(s-s)}$P micelles with various DHA modification (0, 10, 20, 40 mol %) at the concentration of 0.5 mg copolymers/well under D-glucose-free medium. To investigate the mechanism of internalization, the cells were preincubated with PBS added with various inhibitors,[41] including 10 mM D-glucose as GLUT1 transporter inhibitor or 2.5 $\mu$M phenylarine oxide (PhO), 0.5 $\mu$g/mL filipin complex (Fil), and 2.5 $\mu$M colchicines (Col) as endocytic inhibitors, respectively. After 15 min preincubation, Red-BODI-PY-labeled DHA-P$Lys_{(s-s)}$P micelles with 40 mol % of DHA modification (0.5 mg copolymers/well) were introduced to the cells for 30 min at 37 or 4 °C. After 30 min incubation, the medium was removed, and the cells were washed with cold PBS three times and then visualized under an IX2-RFACA fluorescent microscope (Olympus, Osaka, Japan).

**Tumor Implantation.** All animal experiments were carried out in accordance with guidelines evaluated and approved by the ethics committee of Fudan University, Shanghai, China. Glioma-bearing mice were prepared by intracranial injection (striatum, 1.8 mm right lateral to the bregma and 3 mm of depth) of $1 \times 10^5$ U87 cells suspended in 5 $\mu$L of serum-free media into male nude mice with a body weight of 20—25 g (Sina-British Sippr/BK Lab Animal Ltd.). More than 95% of mice could recover from the surgery, and the incidence of glioma was almost 100%.

**Nanoparticle Distribution in Glioma-Bearing Mice.** At the 18th day after implantation, glioma-bearing mice were injected intravenously with Red-BODIPY-labeled P$Lys_{(s-s)}$P or DHA-P$Lys_{(s-s)}$P micelles through the tail vein at the same dose of 1 mg of micelles per animal. Then at 1, 2, 8, and 12 h after administration, the mice were anesthetized and visualized by a Cambridge Research & Instrumentation in vivo imaging system (CRi, MA, USA). After that, mice were sacrificed, and the glioma-bearing brains and other principal organs (heart, liver, spleen, lung, and kidney) were excised carefully to compare relative accumulation. The excised glioma-bearing brains were then fixed in 4% paraformaldehyde for 48 h and further dehydrated in sucrose solution. Afterward, excised brains were frozen at −80 °C in OCT embedding medium (Sakura, Torrance, CA, USA). Frozen sections of 20 $\mu$m thickness were prepared with a cryotome

Cryostat (Leica, CM 1900, Wetzlar, Germany) and stained with 300 nM DAPI for 10 min at room temperature. After being washed twice with PBS pH 7.4, the sections were immediately observed under the IX2-RFACA fluorescent microscope (Olympus, Osaka, Japan) and confocal laser scanning microscope (Olympus, Fluoview FV100, Japan).

**Cell Viability Assay.** The cell viability was assessed by 3-(4,5-dimethylthiazol-2-yl)-2,5-diphenyltetrazolium bromide (MTT; Sigma). U87 cells were seeded in 96-well culture plates (Corning-Coaster, Tokyo, Japan) at a density of $5 \times 10^3$ cells/well. When 60–70% confluence was achieved, the cells were balanced with glucose-free medium for 15 min. Then the cells were incubated with Taxol, PLysP/PTX, DHA-PLysP/PTX, PLys$_{(s-s)}$P/PTX, or DHA-PLys$_{(s-s)}$P/PTX micelles at PTX concentrations ranging from 100 nM to 500 $\mu$M at 37 °C for 48 h in DMEM (added with 2.5 mM D-glucose). After incubation, the medium was removed and the cells were rinsed with cold PBS three times. Subsequently, the *in vitro* cytotoxicity was determined by MTT assay ($n = 4$).

**Cell Cycle Determination.** The progression of cell cycle and apoptosis was determined by flow cytometry *via* propidium iodide (PI; Sigma-Aldrich, MO, USA) staining.[47] U87 cells were seeded in 12-well plates at a density of $10^5$ cells/well. After being prebalanced with glucose-free medium, the cells were incubated with 200 $\mu$L of Taxol, PLysP/PTX, DHA-PLysP/PTX, PLys$_{(s-s)}$P/PTX, or DHA-PLys$_{(s-s)}$P/PTX micelle solution at 1 $\mu$M PTX. The cells treated with saline were used as control. Two hours later, the drug solutions were displaced by ECCM for another 48 h incubation. Then the cells were harvested by a trypsinization method, washed with PBS twice, and incubated with PI solution in an ice bath for 15 min. The cells were collected by centrifugation at 3000 rpm for 15 min at 4 °C. Then the stained cells (10 000 cells) of each sample were detected by FACS Calibur flow cytometer (BD, USA), and the percentage of cell cycle phases and apoptosis was analyzed using Flowjo 6.0.

**Cell Apoptosis Analysis.** The imaging of cell apoptosis was evaluated by PI and Annexin V-FITC (Invitrogen, NY, USA) staining. Briefly, after incubation with Taxol, PLysP/PTX, DHA-PLysP/PTX, PLys$_{(s-s)}$P/PTX, or DHA-PLys$_{(s-s)}$P/PTX micelle solution at a dose of 1 $\mu$M PTX, the U87 cells were further cultured with drug-free ECCM. After another 48 h incubation, the cells were rinsed by cold PBS twice and stained with a cell apoptosis kit (250 $\mu$L binding buffer, 2.5 $\mu$L Annexin V-FITC, and 2.5 $\mu$L PI/well), according to the protocols. Fifteen minutes later, the cells were washed twice and immediately observed under an IX2-RFACA fluorescent microscope (Olympus, Osaka, Japan).

**Evaluation of Anti-tumor Efficacy *in Vivo*.** Intracranial glioma-bearing mice were randomly divided into six groups ($n = 15$) and treated with Taxol, PLysP/PTX, DHA-PLysP/PTX, PLys$_{(s-s)}$P/PTX, or DHA-PLys$_{(s-s)}$P/PTX micelles at a dose of 10 mg PTX/kg *via* intravenous injection at days 12, 15, and 18, respectively (the implantation day was day 0). The mice treated with saline were considered as the control. The treatment experiment was performed with all mice at the same time.

For *in vivo* apoptosis imaging, at day 21, the animals of Taxol, PLys$_{(s-s)}$P/PTX, or DHA-PLys$_{(s-s)}$P/PTX micelle treated groups received intravenously 100 $\mu$L/mouse apoptotic agent Annexin-Vivo 750 (GE Healthcare, USA), which was able to bind to apoptotic cells and reveal information about immediate cell death induced by drug accumulation. Imaging was conducted at 24 h post-Annexin administration by a CRi *in vivo* imaging system (excited at 740 nm; emission collected at 780 nm). After that, the excised glioma-bearing brains were frozen sectioned and stained with DAPI, then observed under the fluorescent microscope. To further validate the apoptotic signal, *in vivo* TUNEL assay was applied to detect the broken nuclear DNA fragments, stained with DAPI, and observed under the fluorescent microscope.

For survival study, all groups were inspected twice daily. All animals were observed for a total period postimplantation of 50 days, and body weight was recorded every 2 days. Each group included 12 mice.

**Statistical Analysis.** Analysis was performed with the computer program GraphPad Prism software. The data are expressed as mean ± SD. Statistical analysis of comparison was done by Student's tests. The comparative survival rates were analyzed by a log rank test.

*Conflict of Interest:* The authors declare no competing financial interest.

*Supporting Information Available:* Synthetic schemes of copolymers and the IR characterization of copolymers. This material is available free of charge *via* the Internet at http://pubs.acs.org.

## REFERENCES AND NOTES

1. Brown, M.; Schrot, R.; Bauer, K.; Dodge, J. Incidence of First Primary Central Nervous System Tumors in California, 2001−2005: Children, Adolescents and Teens. *J. Neurooncol.* **2009**, *94*, 263–273.
2. Agarwal, S.; Sane, R.; Oberoi, R.; Ohlfest, J. R.; Elmquist, W. F. Delivery of Molecularly Targeted Therapy to Malignant Glioma, a Disease of the Whole Brain. *Expert Rev. Mol. Med.* **2011**, *13*, 1–27.
3. Pardridge, W. M. The Blood-Brain Barrier: Bottleneck in Brain Drug Development. *NeuroRx* **2005**, *2*, 3–14.
4. Pardridge, W. M. Blood-Brain Barrier Delivery. *Drug Discovery Today* **2007**, *12*, 54–61.
5. Zhan, C.; Lu, W. The Blood-Brain/Tumor Barriers: Challenges and Chances for Malignant Gliomas Targeted Drug Delivery. *Curr. Pharm. Biotechnol.* **2012**, *13*, 2380–2387.
6. Allhenn, D.; Boushehri, M. A.; Lamprecht, A. Drug Delivery Strategies for the Treatment of Malignant Gliomas. *Int. J. Pharm.* **2012**, *436*, 299–310.
7. Gabathuler, R. Approaches To Transport Therapeutic Drugs across the Blood-Brain Barrier To Treat Brain Diseases. *Neurobiol. Dis.* **2010**, *37*, 48–57.
8. Scherrmann, J. M. Drug Delivery to Brain *via* the Blood-Brain Barrier. *Vasc. Pharmacol.* **2002**, *38*, 349–354.
9. Chen, H.; Zhao, Y.; Wang, H.; Nie, G.; Nan, K. Co-delivery Strategies Based on Multifunctional Nanocarriers for Cancer Therapy. *Curr. Drug Metab.* **2012**, *13*, 1087–1096.
10. Airley, R. E.; Mobasheri, A. Hypoxic Regulation of Glucose Transport, Anaerobic Metabolism and Angiogenesis in Cancer: Novel Pathways and Targets for Anticancer Therapeutics. *Chemotherapy* **2007**, *53*, 233–256.
11. de Boer, A. G.; van der Sandt, I. C.; Gaillard, P. J. The Role of Drug Transporters at the Blood-Brain Barrier. *Annu. Res. Pharmacol. Toxicol.* **2003**, *43*, 629–656.
12. Qin, Y.; Fan, W.; Chen, H.; Yao, N.; Tang, W.; Tang, J.; Yuan, W.; Kuai, R.; Zhang, Z.; Wu, Y.; *et al. In Vitro* and *In Vivo* Investigation of Glucose-Mediated Brain-Targeting Liposomes. *J. Drug Target* **2010**, *18*, 536–549.
13. Xie, F.; Yao, N.; Qin, Y.; Zhang, Q.; Chen, H.; Yuan, M.; Tang, J.; Li, X.; Fan, W.; Zhang, Q.; *et al.* Investigation of Glucose-Modified Liposomes Using Polyethylene Glycols with Different Chain Lengths as the Linkers for Brain Targeting. *Int. J. Nanomed.* **2012**, *7*, 163–175.
14. Li, J.; Zhou, L.; Ye, D.; Huang, S.; Shao, K.; Huang, R.; Han, L.; Liu, Y.; Liu, S.; Ye, L.; *et al.* Choline-Derivate-Modified Nanoparticles for Brain-Targeting Gene Delivery. *Adv. Mater.* **2011**, *23*, 4516–4520.
15. Jiang, X.; Xin, H.; Ren, Q.; Gu, J.; Zhu, L.; Du, F.; Feng, C.; Xie, Y.; Sha, X.; Fang, X. Nanoparticles of 2-Deoxy-D-Glucose Functionalized Poly(ethylene glycol)-*co*-Poly(trimethylene carbonate) for Dual-Targeted Drug Delivery in Glioma Treatment. *Biomaterials* **2014**, *35*, 518–529.
16. Wood, I. S.; Trayhurn, P. Glucose Transporters (GLUT and SGLT): Expanded Families of Sugar Transport Proteins. *Br. J. Nutr.* **2003**, *89*, 3–9.
17. Warburg, O. *Science* **1956**, *123*, 309–314.

18. Vander Heiden, M. G. Targeting Cancer Metabolism: A Therapeutic Window Opens. *Nat. Rev. Drug Discovery* **2011**, *10*, 671–684.

19. Calvaresi, E. C.; Granchi, C.; Tuccinardi, T.; Di Bussolo, V.; Huigens, R. W., III; Lee, H. Y.; Palchaudhuri, R.; Macchia, M.; Martinelli, A.; Minutolo, F.; *et al.* Dual Targeting of the Warburg Effect with a Glucose-Conjugated Lactate Dehydrogenase Inhibitor. *ChemBioChem* **2013**, *14*, 2263–2267.

20. Luo, F.; Liu, X.; Yan, N.; Li, S.; Cao, G.; Cheng, Q.; Xia, Q.; Wang, H. Hypoxia-Inducible Transcription Factor-1α Promotes Hypoxia-Induced A549 Apoptosis *via* a Mechanism That Involves the Glycolysis Pathway. *BMC Cancer* **2006**, *6*, 26–35.

21. Koff, S. G.; Sterbis, J. R.; Davison, J. M.; Montilla-Soler, J. L. A Unique Presentation of Appendicitis: F-18 FDG PET/CT. *Clin. Nucl. Med.* **2006**, *31*, 704–706.

22. Agus, D. B.; Vera, J. C.; Golde, D. W. Stromal Cell Oxidation: A Mechanism by Which Tumors Obtain Vitamin C. *Cancer Res.* **1999**, *59*, 4555–4558.

23. Rumsey, S. C.; Kwon, O.; Xu, G. W.; Burant, C. F.; Simpson, I.; Levine, M. Glucose Transporter Isoforms GLUT 1 and GLUT 3 Transport Dehydroascorbic Acid. *J. Biol. Chem.* **1997**, *272*, 18982–18989.

24. Corpe, C. P.; Lee, J. H.; Kwon, O.; Eck, P.; Narayanan, J.; Kirk, K. L.; Levine, M. 6-Bromo-6-deoxy-L-ascorbic Acid: An Ascorbate Analog Specific for $Na^+$-Dependent Vitamin C Transporter but Not Glucose Transporter Pathways. *J. Biol. Chem.* **2005**, *280*, 5211–5220.

25. McCarty, M. F. Expression and/or Activity of the SVCT2 Ascorbate Transporter May Be Decreased in Many Aggressive Cancers, Suggesting Potential Utility for Sodium Bicarbonate and Dehydroascorbic Acid in Cancer Therapy. *Med. Hypotheses* **2013**, *81*, 664–670.

26. Agus, D. B.; Gambhir, S. S.; Pardridge, W. M.; Spielholz, C.; Baselga, J.; Vera, J. C.; Golde, D. W. Vitamin C Crosses the Blood-Brain Barrier in the Oxidized Form through the Glucose Transporters. *J. Clin. Invest.* **1997**, *100*, 2842–2848.

27. Airley, R. E.; Mobasheri, A. Hypoxic Regulation of Glucose Transport, Anaerobic Metabolism and Angiogenesis in Cancer: Novel Pathways and Targets for Anticancer Therapeutics. *Chemotherapy* **2007**, *53*, 233–256.

28. Bourzac, K. Nanotechnology: Carrying Drugs. *Nature* **2012**, *491*, S58–S60.

29. Hemant, S. Overcoming the Challenges in the Effective Delivery of Chemotherapies to CNS Solid Tumors. *Ther. Delivery* **2010**, *1*, 289–305.

30. Wu, G.; Fang, Y. Z.; Yang, S.; Lupton, J. R.; Turner, N. D. Glutathione Metabolism and Its Implications for Health. *J. Nutr.* **2004**, *134*, 489–492.

31. Samarajeewa, S.; Shrestha, R.; Elsabahy, M.; Karwa, A.; Li, A.; Zentay, R. P.; Kostelc, J. G.; Dorshow, R. B.; Wooley, K. L. *In Vitro* Efficacy of Paclitaxel-Loaded Dual-Responsive Shell Cross-Linked Polymer Nanoparticles Having Orthogonally Degradable Disulfide Cross-Linked Corona and Polyester Core Domains. *Mol. Pharmacol.* **2013**, *10*, 1092–1099.

32. Bae, K. H.; Mok, H.; Park, T. G. Synthesis, Characterization, and Intracellular Delivery of Reducible Heparin Nanogels for Apoptotic Cell Death. *Biomaterials* **2008**, *29*, 3376–3383.

33. Lallana, E.; Fernandez-Trillo, F.; Sousa-Herves, A.; Riguera, R.; Fernandez-Megia, E. Click Chemistry with Polymers, Dendrimers, and Hydrogels for Drug Delivery. *Pharm. Res.* **2012**, *29*, 902–921.

34. Koo, A. N.; Lee, H. J.; Kim, S. E.; Chang, J. H.; Park, C.; Kim, C.; Park, J. H.; Lee, S. C. Disulfide-Cross-Linked PEG-Poly(amino acid)s Copolymer Micelles for Glutathione-Mediated Intracellular Drug Delivery. *Chem. Commun.* **2008**, *28*, 6570–6572.

35. Koo, A. N.; Min, K. H.; Lee, H. J.; Lee, S. U.; Kim, K.; Kwon, I. C.; Cho, S. H.; Jeong, S. Y.; Lee, S. C. Tumor Accumulation and Antitumor Efficacy of Docetaxel-Loaded Core-Shell-Corona Micelles with Shell-Specific Redox-Responsive Cross-Links. *Biomaterials* **2012**, *33*, 1489–1499.

36. Iyer, S. S.; Anderson, A. S.; Reed, S.; Swanson, B.; Schmidt, J. G. Synthesis of Orthogonal End Functionalized Oligoethylene Glycols of Defined Lengths. *Tetrahedron Lett.* **2004**, *45*, 4285–4288.

37. Deming, T. J. Facile Synthesis of Block Copolypeptides of Defined Architecture. *Nature* **1997**, *390*, 386–389.

38. Bach, L. G.; Islam, M. R.; Nga, T. T.; Binh, M. T.; Hong, S. S.; Gal, Y. S.; Lim, K. T. Chemical Modification of Polyhedral Oligomeric Silsesquioxanes by Functional Polymer *via* Azide−Alkyne Click Reaction. *J. Nanosci. Nanotechnol.* **2013**, *13*, 1970–1973.

39. Gindy, M. E.; Ji, S.; Hoye, T. R.; Panagiotopoulos, A. Z.; Prud'homme, R. K. Preparation of Poly(ethylene glycol) Protected Nanoparticles with Variable Bioconjugate Ligand Density. *Biomacromolecules* **2008**, *9*, 2705–2711.

40. Towner, R. A.; Gillespie, D. L.; Schwager, A.; Saunders, D. G.; Smith, N.; Njoku, C. E.; Krysiak, R. S.; Larabee, C.; Iqbal, H.; Floyd, R. A.; *et al.* Regression of Glioma Tumor Growth in F98 and U87 Rat Glioma Models by the Nitrone OKN-007. *Neuro. Oncol.* **2013**, *15*, 330–340.

41. Ke, W.; Shao, K.; Huang, R.; Han, L.; Liu, Y.; Li, J.; Kuang, Y.; Ye, L.; Lou, J.; Jiang, C. Gene Delivery Targeted to the Brain Using an Angiopep-Conjugated Polyethyleneglycol-Modified Polyamidoamine Dendrimer. *Biomaterials* **2009**, *30*, 6976–6985.

42. Bottsford-Miller, J. N.; Coleman, R. L.; Sood, A. K. Resistance and Escape from Antiangiogenesis Therapy: Clinical Implications and Future Strategies. *J. Clin. Oncol.* **2012**, *30*, 4026–4034.

43. Yang, L.; Lin, C.; Wang, L.; Guo, H.; Wang, X. Hypoxia and Hypoxia-Inducible Factors in Glioblastoma Multiforme Progression and Therapeutic Implications. *Exp. Cell Res.* **2012**, *318*, 2417–2426.

44. Shimanishi, M.; Ogi, K.; Sogabe, Y.; Kaneko, T.; Dehari, H.; Miyazaki, A.; Hiratsuka, H. Silencing of GLUT-1 Inhibits Sensitization of Oral Cancer Cells to Cisplatin during Hypoxia. *J. Oral Pathol. Med.* **2013**, *42*, 382–388.

45. Lalatsa, A.; Schätzlein, A. G.; Mazza, M.; Le, T. B.; Uchegbu, I. F. Amphiphilic Poly(L-amino acids): New Materials for Drug Delivery. *J. Controlled Release* **2012**, *161*, 523–536.

46. Vivero-Escoto, J. L.; Taylor-Pashow, K. M.; Huxford, R. C.; Della, R. J.; Okoruwa, C.; An, H.; Lin, W.; Lin, W. Multifunctional Mesoporous Silica Sanospheres with Cleavable Gd(III) Chelates as MRI Contrast Agents: Synthesis, Characterization, Target-Specificity, and Renal Clearance. *Small* **2011**, *7*, 3519–3528.

47. Zhan, C. Y.; Wei, X.; Qian, J.; Feng, L.; Zhu, J.; Lu, W. Co-delivery of TRAIL Gene Enhances the Anti-glioblastoma Effect of Paclitaxel *in Vitro* and *in Vivo*. *J. Controlled Release* **2012**, *160*, 630–636.

48. Tao, Y.; Ning, M.; Dou, H. A Novel Therapeutic System for Malignant Glioma: Nanoformulation, Pharmacokinetic, and Anticancer Properties of Cell-Nano-Drug Delivery. *Nanomedicine* **2013**, *9*, 222–232.

49. Yoshizawa, Y.; Kono, Y.; Ogawara, K.; Kimura, T.; Higaki, K. PEG Liposomalization of Paclitaxel Improved Its *In Vivo* Disposition and Anti-tumor Efficacy. *Int. J. Pharm.* **2011**, *412*, 132–141.

50. Abou El Hassan, M. A.; Braam, S. R.; Kruyt, F. A. Paclitaxel and Vincristine Potentiate Adenoviral Oncolysis That Is Associated with Cell Cycle and Apoptosis Modulation, Whereas They Differentially Affect the Viral Life Cycle in Non-Small-Cell Lung Cancer Cells. *Cancer Gene Ther.* **2006**, *13*, 1105–1114.

51. Lee, J. H.; Na, K.; Song, S. C.; Lee, J.; Kuh, H. J. The Distribution and Retention of Paclitaxel and Doxorubicin in Multicellular Layer Cultures. *Oncol. Rep.* **2012**, *27*, 995–1002.

52. Schutters, K.; Reutelingsperger, C. Phosphatidylserine Targeting for Diagnosis and Treatment of Human Diseases. *Apoptosis* **2010**, *15*, 1072–1082.

53. Huang, S.; Shao, K.; Liu, Y.; Kuang, Y.; Li, J.; An, S.; Guo, Y.; Ma, H.; Jiang, C. Tumor-Targeting and Microenvironment-Responsive Smart Nanoparticles for Combination Therapy of Antiangiogenesis and Apoptosis. *ACS Nano* **2013**, *7*, 2860–2871.

54. Gu, G.; Gao, X.; Hu, Q.; Kang, T.; Liu, Z.; Jiang, M.; Miao, D.; Song, Q.; Yao, L.; Tu, Y.; *et al.* The Influence of the Penetrating Peptide iRGD on the Effect of Paclitaxel-Loaded MT1-AF7p-Conjugated Nanoparticles on Glioma Cells. *Biomaterials* **2013**, *34*, 5138–5148.

55. Daly, W. H.; Poche, D. The Preparation of *N*-Carboxyanhydrides of α-Amino Acids Using Bis(trichloromethyl)-carbonate. *Tetrahedron Lett.* **1988**, *29*, 5859–5862.

56. Marra, A.; Vecchi, A.; Chiappe, C.; Melai, B.; Dondoni, A. Validation of the Copper(I)-Catalyzed Azide—Alkyne Coupling in Ionic Liquids. Synthesis of a Triazole-Linked C-Disaccharide as a Case Study. *J. Org. Chem.* **2008**, *73*, 2458–2461.